NASA/TM–20250000605

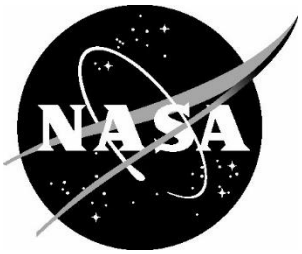

Structural Analysis of Load-Bearing Components in Mars Science Helicopter

Dorcas V. Kaweesa
NASA Ames Research Center, Moffett Field, CA

Joshua Bowman
Science and Technology Corporation, NASA Ames Research Center, Moffett Field, CA

January 2025

NASA STI Program Report Series

Since its founding, NASA has been dedicated to the advancement of aeronautics and space science. The NASA scientific and technical information (STI) program plays a key part in helping NASA maintain this important role.

The NASA STI program operates under the auspices of the Agency Chief Information Officer. It collects, organizes, provides for archiving, and disseminates NASA's STI. The NASA STI program provides access to the NTRS Registered and its public interface, the NASA Technical Reports Server, thus providing one of the largest collections of aeronautical and space science STI in the world. Results are published in both non-NASA channels and by NASA in the NASA STI Report Series, which includes the following report types:

- TECHNICAL PUBLICATION. Reports of completed research or a major significant phase of research that present the results of NASA Programs and include extensive data or theoretical analysis. Includes compilations of significant scientific and technical data and information deemed to be of continuing reference value. NASA counterpart of peer-reviewed formal professional papers but has less stringent limitations on manuscript length and extent of graphic presentations.

- TECHNICAL MEMORANDUM. Scientific and technical findings that are preliminary or of specialized interest, e.g., quick release reports, working papers, and bibliographies that contain minimal annotation. Does not contain extensive analysis.

- CONTRACTOR REPORT. Scientific and technical findings by NASA-sponsored contractors and grantees.

- CONFERENCE PUBLICATION. Collected papers from scientific and technical conferences, symposia, seminars, or other meetings sponsored or co-sponsored by NASA.

- SPECIAL PUBLICATION. Scientific, technical, or historical information from NASA programs, projects, and missions, often concerned with subjects having substantial public interest.

- TECHNICAL TRANSLATION. English-language translations of foreign scientific and technical material pertinent to NASA's mission.

Specialized services also include organizing and publishing research results, distributing specialized research announcements and feeds, providing information desk and personal search support, and enabling data exchange services.

For more information about the NASA STI program, see the following:

- Access the NASA STI program home page at http://www.sti.nasa.gov

- .

NASA/TM–20250000605

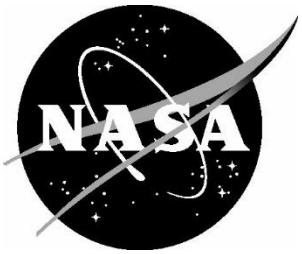

Structural Analysis of Load-Bearing Components in Mars Science Helicopter

Dorcas V. Kaweesa
NASA Ames Research Center, Moffett Field, CA

Joshua Bowman
Science and Technology Corporation, NASA Ames Research Center, Moffett Field, CA

National Aeronautics and
Space Administration

Ames Research Center
Moffett Field, CA

January 2025

Available from:

NASA STI Program / Mail Stop 050
NASA Langley Research Center
Hampton, VA 23681-2199

Nomenclature

MSH	=	Mars Science Helicopter
MAC	=	Mass Acceleration Curve, kg
f_n	=	Beam Natural Frequency, Hz
M_p	=	Point Mass, End of Beam, kg
M_b	=	Mass of Beam, Evenly Distributed, kg
E	=	Elastic Modulus of Beam, Pa
I	=	Area Moment of Inertia of Beam, m^4
L	=	Length of Beam, m

Abstract

The successful demonstration of powered flight on Mars by Ingenuity has led to the development of next generation Martian rotorcraft. As technology advances from a technology demonstrator to possible expanded planetary science investigations, the potential to fly a high payload carrying rotorcraft relies on the capability to analyze and validate the structural integrity of the vehicle in addition to the rotor aerodynamic performance. The Mars Science Helicopter (MSH), a next generation hexacopter concept, is an example of a proposed vehicle that would perform science investigations independent of a land-based vehicle. To ensure the feasibility and viability of MSH mission performance, it is critical to mature the structural design of vehicle concepts to bridge the gap between the best practices of the spacecraft and aircraft communities. MSH was analyzed under operational and 26G quasi-static launch loads with different rotor arm and frame designs. Structural analysis results showed that rotor arms could be stiffened for significantly improved structural performance with minimal mass penalty, while the rotorcraft frame exhibited a more complex relationship between mass and launch load stresses due to the mass-dependent launch loads.

I. Introduction

Ingenuity is the first and only extra-terrestrial rotorcraft with flight heritage to date [1]. The rotorcraft's groundbreaking success demonstrated the power of aerial mobility and capability of Mars exploration over its last three years of flight. Following Ingenuity's successful flights, next-generation rotorcraft for future Mars exploration will extend from technology demonstration to being instrumented with dedicated payload for science investigations [2, 3, 4]. This will require the development of heavier vehicles to accommodate dedicated science payloads for future missions. A series of advanced rotorcraft designs have been conceptualized [5]. One example is the Mars Science Helicopter (MSH), a next-generation vehicle design concept designed to be capable of performing planetary exploration and conducting high-value science tasks (Figure 1) [6, 7, 8]. MSH is designed to carry about 5kg of dedicated science payload over altitudes and ranges an order of magnitude farther than Ingenuity's flight range (approximately 17km) and highest altitude (approximately 24m) attained over the course of 72 flights. Ingenuity has provided heritage for the design process used to develop MSH. Some notable differences, however, are the mass, vehicle's structural design, and rotor configuration. For comparison, Ingenuity's total vehicle mass was 1.8kg, since it carried no dedicated science payload, and the MSH configuration assumed for this study had a nominal mass of ~31kg. Ingenuity had a coaxial two-bladed rotor configuration whereas MSH uses a hexacopter six-bladed rotor configuration.

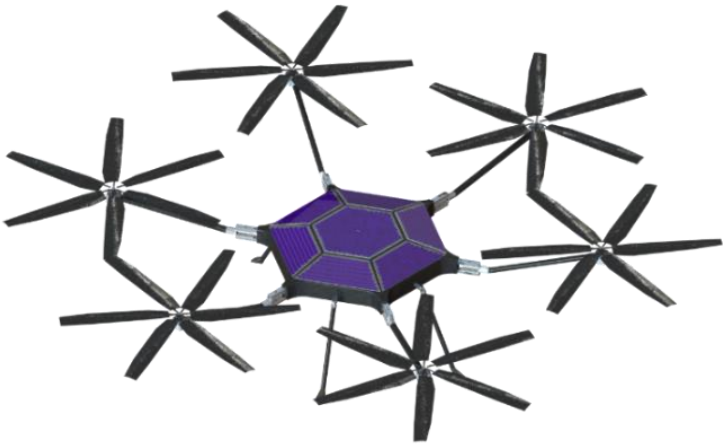

Figure 1. Next-generation conceptual Mars Science Helicopter (MSH) capable of carrying ~5kg of dedicated science payload

The expansion of a Martian rotorcraft from an Ingenuity-class vehicle to a high-payload carrying vehicle requires new vehicle structural design to accommodate the additional weight from the instrumentation and science payload. To successfully enable science investigations, MSH will also require more efficient blade aerodynamic performance [9, 10], an optimized light weight structural design, and improved handling qualities and flight control on Mars [11]. Additionally, a viable control system for such a vehicle must be identified to capture the rotorcraft dynamics in real-time. The MSH concept design has undergone structural analysis to estimate the structural mass required to achieve optimal lightweight structural properties especially for the load-bearing components: the six rotor arms and the frame/fuselage. This paper focuses on addressing the structural analysis of these two major load-bearing components performed via finite elements analyses using Abaqus/CAE©. The main objective is to understand the structural behavior of the load-bearing components based on different design and load conditions by assessing the structural stress and normal modes under launch loads and operational loads. For launch, the cantilevered rotor arms are folded to properly stow into a Pathfinder-sized aeroshell. To add additional support during launch, MSH has supports on the frame/fuselage to which the rotor arms are fastened when in the stowed configuration. These supports are not used in the deployed configuration, as the arms must unfold to their final position. The two rotorcraft configurations, deployed and stowed, are shown in Figure 2.

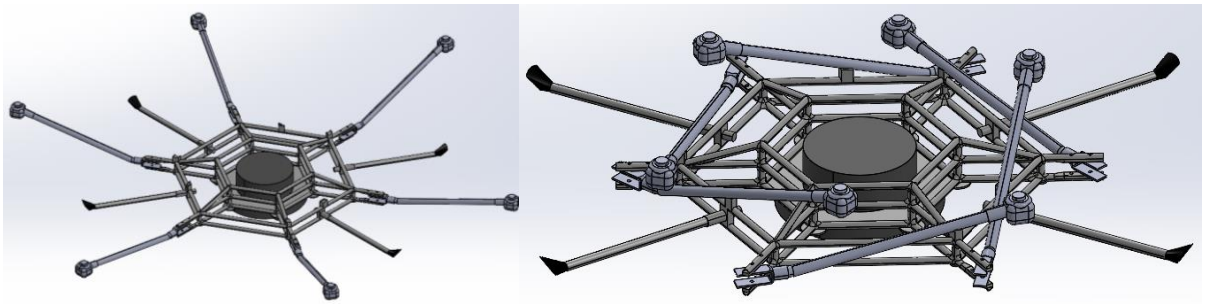

Figure 2. CAD model rendition of deployed (left) and stowed (right) MSH configurations

II. MSH Rotor Arm Study

The first MSH load-bearing component analyzed was an isolated rotor arm assembly. The goal for studying the rotor arm, shown in Figure 3, was to determine how different numbers of axial stiffeners with varying diameters and varying wall thicknesses of the arm can impact the overall mass of the rotor arm, the quasistatic stress, and the natural frequency of the arm, particularly the flap and lag frequency modes. In this case, the flap and lag frequency modes denote the translation of the arm in the vertical and lateral directions respectively. While the original, simple tube design of the arms served as a preliminary structure, the inclusion of these stiffeners and variation in wall thickness can improve structural performance without significant increases in mass. The addition of stiffeners within the arm cylinder was inspired by the Ingenuity rotor mast design.

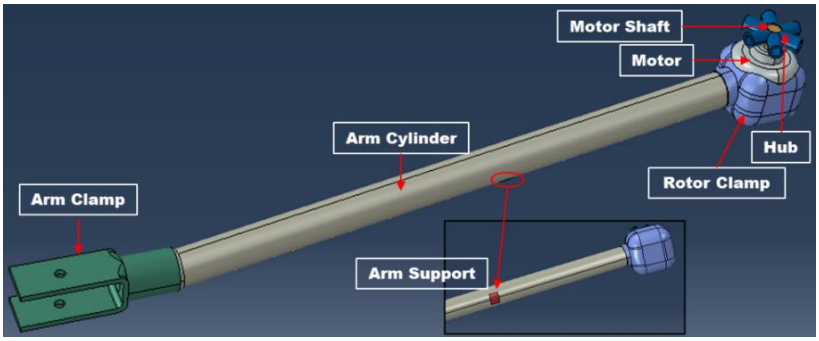

Figure 3. CAD model rendition of an isolated rotor arm assembly

The rotor blades were excluded from the rotor arm analysis since the introduction of their separate modes made results more difficult to interpret and required significantly longer analysis times. Future work will focus on the structural analysis of the blades separately. To simulate the effect of the blade mass at the end of the arm without introducing their separate frequency modes, the blade mass of 0.17kg per blade (6 blades per rotor) was added to the motor/rotor subassembly which has a mass of 0.2kg (this includes the motor, motor shaft, and hub), thus increasing the total motor/blade subassembly mass to 1.22kg. For predicting the impact of launch loads, a representative arm support was placed on the bottom end of the arm cylinder to represent the supported arm assembly in the stowed configuration. The representative arm support was defined to have infinite stiffness and near zero mass. The infinite stiffness allowed the static structural simulation of the quasistatic 26G with the arm being supported in the same manner as in the full MSH structure when in the stowed configuration without introducing elastic behavior of the support. The near-zero mass of the arm support implied that there was a negligible effect on the natural frequency of the arm or operational loads in the deployed configuration, as the support would not be in contact with the arm in the deployed configuration. The mass of the arm cylinder changed with the addition of different sized stiffeners, but the mass of other subcomponents was kept constant. The materials selected for the subcomponents of the isolated arm assembly are presented in Table 1. The carbon fiber properties assigned to the arm cylinder, rotor and arm clamps, and representative arm support were assumed to have the same properties as the material used in the Ingenuity rotor mast but were considered homogeneous and continuous to simplify the current analysis. As stated above, the mass of the motor, motor shaft, and hub altogether, including the blade masses, was 1.22kg, and the mass of the arm cylinder, arm clamp, and rotor clamp altogether was 0.425kg.

Table 1. Materials assigned to the subcomponents of the rotor arm assembly

Component	Material	Mass (kg)
Arm Cylinder	Carbon fiber (IM7)	Variable
Arm Clamp	Carbon fiber (IM7)	0.0902
Rotor Clamp	Carbon fiber (IM7)	0.182
Motor	Steel	0.976*
Motor Shaft	Steel	0.0493*
Hub	Aluminum (Al6061)	0.195
Custom arm support	Carbon fiber (IM7)	2.83e-7

*Density modified to capture blade mass, but all other properties unchanged

A base case analysis featuring an isolated arm assembly with no stiffeners and the original wall thickness of 1.5mm was performed to obtain the baseline values for the mass, peak quasistatic stress due to a 26G load, and the modal frequency. Different sized stiffeners were added sequentially as reinforcements in the wall of the rotor arm assembly and the mass, peak stress, and modal frequency were recorded for each subsequent case analyzed. The categories of the arm cylinder's wall thicknesses and different sized stiffeners are presented in Table 2.

Two finite element simulation procedures were performed for a series of analyses of a single isolated arm assembly. The first procedure involved a quasistatic stress analysis where the peak stress experienced by the vehicle in the stowed configuration during launch was determined based on a 26G load. It was confirmed that it was more conservative to consider a vertical downward acceleration. In this simulation, fixed boundary conditions were placed on the arm clamp, where the arm would be connected to the frame of MSH, and at the representative arm support, where the arm would be additionally supported in the stowed configuration in the full structure. The rotor arms have a greater level of support when stowed, but the launch loads only occur when the arms are in the stowed configuration.

Table 2. Categories of parameters and variables defined for the arm assembly

Category	Parameters	Variables
1	Wall thickness (mm)	1.5; 2; 2.5
	Number of stiffeners	None
	Stiffener diameters (mm)	None
2	Wall thickness (mm)	1.5
	Number of stiffeners	6; 8; 10; 12
	Stiffener diameters (mm)	0.75; 1.5; 2.25
3	Wall thickness (mm)	2
	Number of stiffeners	6; 8; 10; 12
	Stiffener diameters (mm)	1.5

The Mass Acceleration Curve (MAC) [12] shown in Figure 4 was used to determine the approximate launch load conditions as a 26G quasi-static load. While the nominal 31kg MSH design would indicate that a 20G quasi-static load would be acceptable, additional margin was added due to the early stage of the design process. As such, a 26G quasi-static load was used, bearing in mind that smaller components possibly experience greater acceleration.

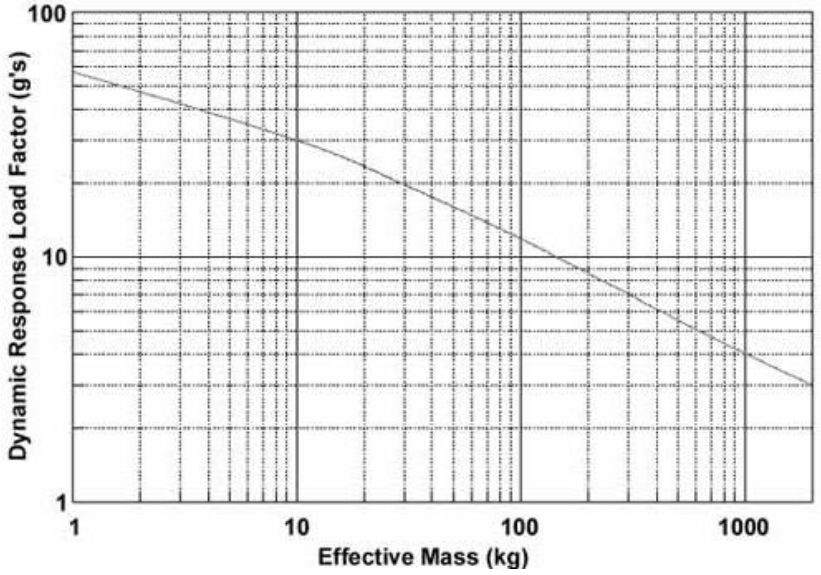

Figure 4. Mass-Acceleration Curve [12]

The second procedure involved a modal frequency analysis where the impact of the rotor arm's natural frequency during deployment was predicted. The same fixed boundary condition on the arm clamp was kept but the fixed condition on the representative arm support was removed to simulate the arm in the deployed configuration for flight operation. This is because the natural frequencies during operation, when the arm assembly is deployed, are the main concern and would inherently be more conservative than the frequencies in the stowed configuration due to the longer lever arm of the deployed arm. Determining the natural frequencies also helped identify whether damping is needed to limit the impact from extensive structural vibrations which will likely be present for heavier Mars rotorcraft.

To further validate and verify the frequency values obtained from the simulation FEA for the isolated arm assembly, hand calculations for natural frequency for a similar structure were used, using Equation 1 extracted from Table 4.8 from *Formulas for Dynamics, Acoustics and Vibration* by Blevins [13]. The hand calculations for the natural frequency were based on the assumptions that the beam is uniform axially, the mass of the beam is distributed, and the beam is straight from a fixed point. The results from the calculations did not match exactly since the arm was angled rather than perpendicular to the fixed end but the results were within 5% of the frequency of the MSH arms from the FEA. The results of the simulations were assessed based on the ratio of natural frequency to mass of the arm. A higher ratio indicated a better performing design of MSH arm as higher frequency and lower mass were desired.

$$f_n = \frac{1}{2\pi}\sqrt{\frac{3EI}{L^3(M_p+0.24M_b)}} \qquad (1)$$

The results from the rotor arm stiffener studies are presented in the succeeding subcategories.

A. MSH Rotor Arm Study – Results

I. Arm Assembly Analysis I: Changes in Wall Thickness, No Stiffeners

As for the first category of analyses, the base case arm assembly, with no stiffeners and a constant 1.5mm wall thickness was analyzed along with two other cases of arm assemblies with

no stiffeners, but with larger wall thicknesses (2mm and 2.5mm). For this, two analysis procedures were undertaken: a quasistatic 26G analysis with the arm assembly in the stowed configuration and a modal frequency analysis with the arm assembly in the deployed configuration. The peak stress experienced in the arm for each case is presented in Table 3.

Table 3. Results for cases of the arm with increasing wall thickness and no stiffeners

Arm Wall Thickness (mm)	Mass (kg) Arm + Arm Clamps Only	Peak Stress (MPa)
1.5	0.4252	480.44
2	0.4742	472.95
2.5	0.5222	386.91

The peak stress was mostly experienced in the region of the arm around the arm support as shown in Figure 5. The arm supports were not included in the original design of the MSH structure, and prior analysis of the arm showed peak stresses that were 29% to 34% higher and areas of high stress concentrations prevalent on the arm clamp in the base of the arm assembly fastened to the frame/fuselage. Therefore, six arm supports were added to the frame to grip the arm assemblies in place while in the stowed configuration. This helped mitigate and reduce the areas of high stress concentrations on the arm. It is also important to note that the mass indicated for each wall thickness in Table 3 only considers the combined mass of arm cylinder, arm clamp, and rotor clamp. The combined mass of the motor, motor shaft, and hub remained constant at 1.22kg for all cases. The total mass of the arm assembly was obtained by adding 1.22kg to the mass of each individual wall thickness case.

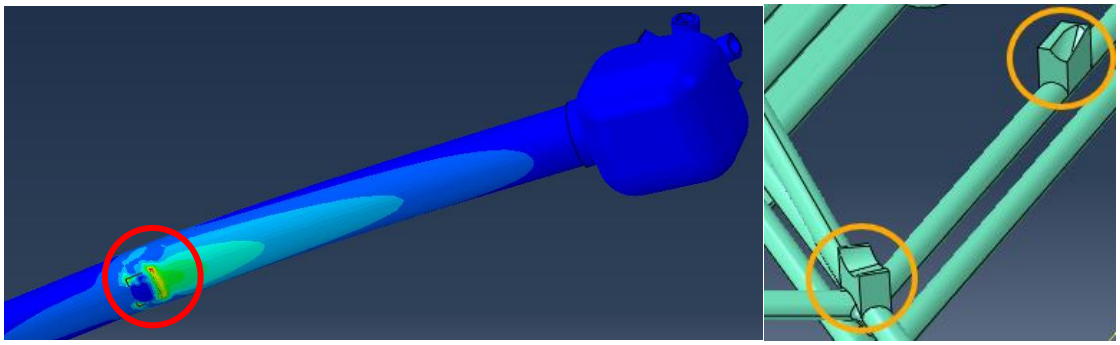

a) b)

Figure 5. a) FEA of the MSH arm assembly showing region around the representative arm support experiencing peak stress, and b) Two arm supports shown on the frame

The modal frequency analysis of the arm assembly was performed to determine the natural frequency of the arms when deployed during flight operation on Mars. Figure 6 shows an example of the lag and flap frequency modes of the deformed rotor arm which denote the modes in the lateral and vertical directions respectively. Varying the wall thickness of the arm not only increased the mass of the entire arm assembly, but as shown in Figure 7, a thicker arm increased the natural frequency in both vertical and lateral directions.

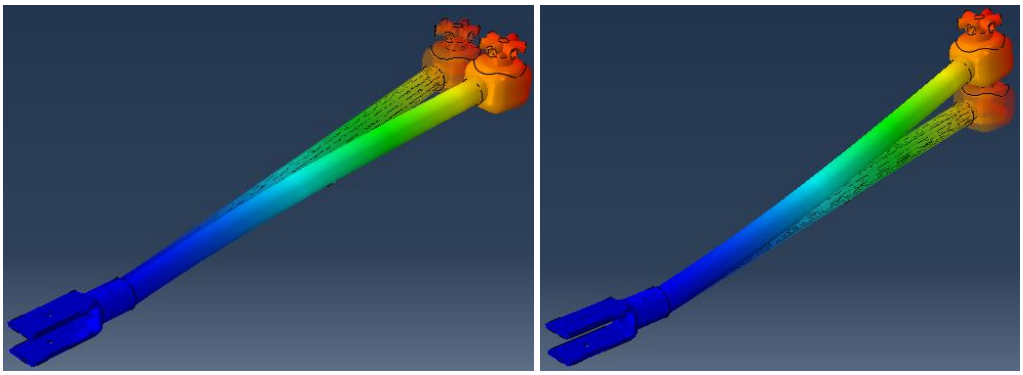

Figure 6. Deformed rotor arm showing frequency modes in the lateral and vertical directions respectively

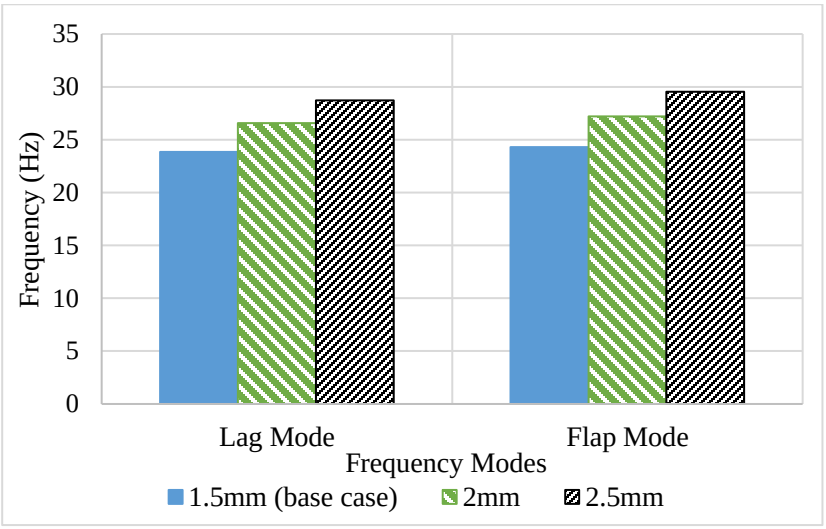

Figure 7. Lag and flap frequency modes of the arm assembly with varying arm wall thicknesses and no stiffeners

To determine optimal performance based on the mass of the arm, the frequency to mass ratio of the arm assembly was calculated. Figure 8 shows the frequency to mass ratios for both lag and flap frequency modes in the lateral and vertical directions respectively. A higher frequency to mass ratio indicated better performance and design of the MSH rotor arm from a mass efficiency perspective. The highest frequency to mass ratios were 56.07Hz/kg in lag mode for the 1.5mm thick arms (base case) and 57.38Hz/kg in flap mode for the 2mm thick arms. While the frequency to mass ratio of the 2mm thick arms slightly outperformed the 1.5mm thick arms in flap mode and the frequency to mass ratio of the 1.5mm thick arms slightly outperformed the 2mm thick arms in lag mode, the percentage difference was slightly worse in the flap mode. As a result, of the three cases analyzed, the 1.5mm thick arms performed the best due to the mass savings in the arm and a higher frequency to mass ratio in the lag mode.

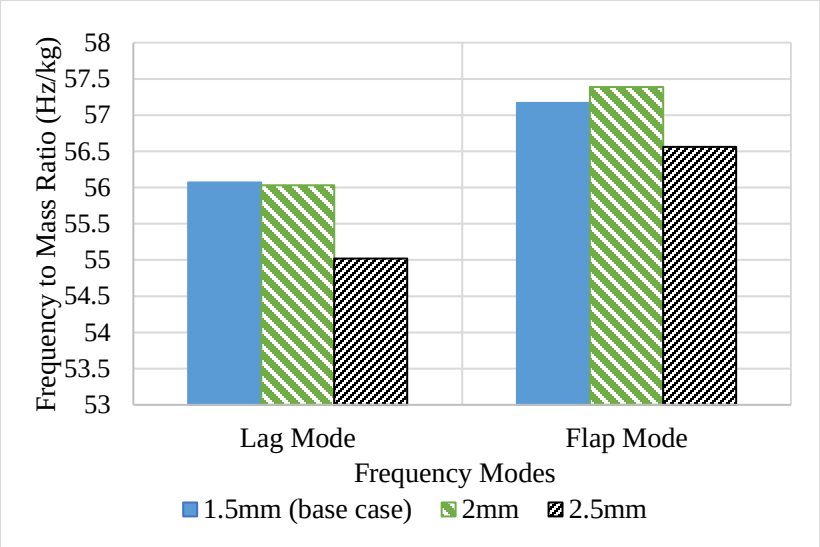

Figure 8. Frequency to mass ratios of the arm assembly with varying arm wall thicknesses and no stiffeners

II. Arm Assembly Analysis II: Constant 1.5mm Thick Arms with Changes in Number of Stiffeners and Stiffener Diameters

The second category of the arm assembly analysis featured cases of the arm with a constant 1.5mm wall thickness, but with varying stiffeners and stiffener diameters as presented in Table 2. The addition of stiffeners as reinforcement in the arm demonstrated the impact on the structural viability with regards to the arm stiffness. Table 4 highlights the changes in the mass and the peak stress variations of the arm assembly as the number of stiffeners increases with varying stiffener diameters increases.

Table 4. Results from the quasistatic and natural frequency analyses of the arm assembly with different numbers of stiffeners and stiffener diameters and 1.5 mm wall thickness

Number of Stiffeners	Stiffener Diameter (mm)	Mass (kg) Arm + Arm Clamps Only	Peak Stress (MPa)	Lag Mode (Hz)	Flap Mode (Hz)
6	0.75	0.436	314.10	24.33	24.81
	1.5	0.450	288.20	25.10	25.64
	2.25	0.471	306.66	26.07	26.67
8	0.75	0.438	233.29	24.46	24.96
	1.5	0.458	305.21	25.48	26.05
	2.25	0.485	354.33	26.73	27.38
10	0.75	0.440	367.81	24.60	25.11
	1.5	0.465	305.02	25.86	26.46
	2.25	0.500	278.17	27.37	28.07
12	0.75	0.443	379.06	24.75	25.26
	1.5	0.472	330.79	26.23	26.84
	2.25	0.514	244.52	28.00	28.74

As visualized in Figure 9, the stress in the arm with six stiffeners fluctuates as the stiffener diameter increases. Additionally, the arm with eight stiffeners shows an increasing trend in stress as the stiffener diameter increased whereas the arm with ten and twelve stiffeners respectively shows a decreasing trend in stress as the stiffener diameter increases. The peak stress varied in the arm assembly as the stiffener diameter increased for each case of number of stiffeners and it is evident that changing the number of stiffeners in the arm assembly does not directly correlate to the decrease in stress. However, adjusting the diameter of the stiffeners changes the mass of the arm which impacts the acceleration loads. As such, the required mass margins dictate the behavior of the structural component since the load applied is mass dependent. The peak stress observed in the various arm assembly cases was prevalent in the region of the arm near the representative arm support. This is the region of the arm that would be connected to the arm support when the arms are in the stowed configuration.

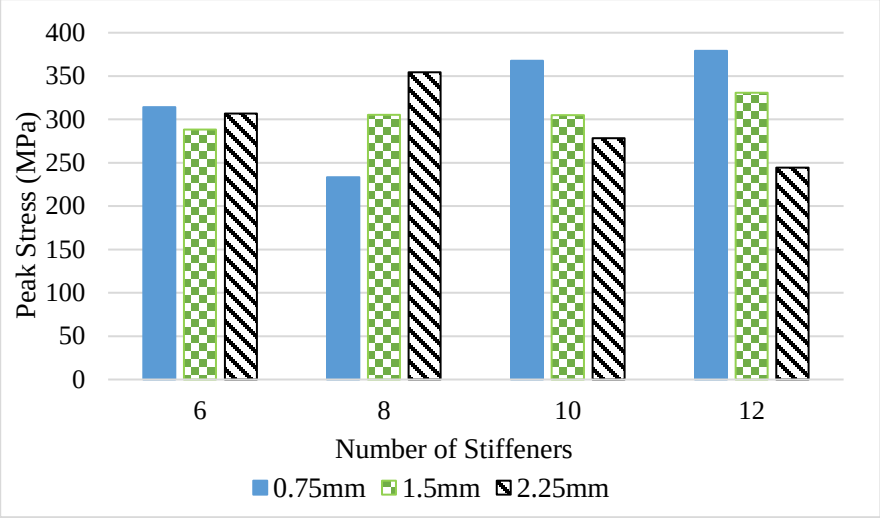

Figure 9. Peak stress trends of the arm assembly with varying arm stiffener diameters

In addition to the quasistatic 26G analysis, the flap and lag frequency modes of the arm were also obtained. As the diameter of the stiffeners increases in each number of stiffener case, both lag and flap frequency modes show an increasing trend. This behavior is dependent on the increase in mass as the diameter for each stiffener increases (Table 4). To identify optimal performance of the arm, the frequency to mass ratio was calculated for each number of stiffener case. The category with the highest frequency to mass ratio was considered superior in performance. Figure 10 and Figure 11 show similar frequency to mass ratio trends for the lag and flap mode trends respectively. The highest frequency to mass ratios were observed in the arm with ten stiffeners and a 0.75mm stiffener diameter with 55.89Hz/kg in lag mode and 57.03Hz/kg in flap mode. Ultimately, the goal for analyzing multiple arm stiffeners with different stiffener diameters was to determine feasible arm design conditions that would provide improved strength and simultaneously minimize mass. As a result, the arm with ten stiffeners with 0.75mm diameter performed best from a rotor arm mass efficiency perspective.

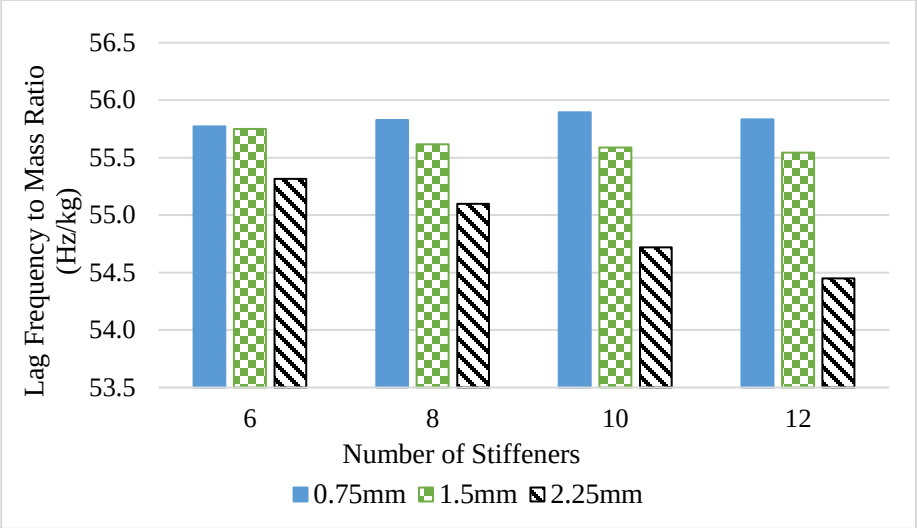

Figure 10. Lag mode frequency to mass ratios for cases of different number of arm stiffeners with varying stiffener diameters

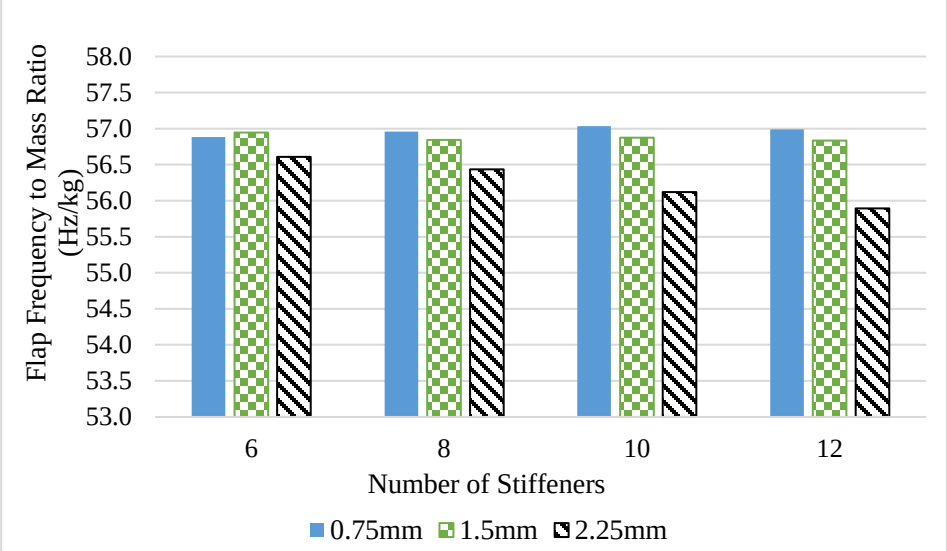

Figure 11. Flap mode frequency to mass ratios for cases of different number of arm stiffeners with varying stiffener diameters

III. Arm Assembly Analysis III: Constant 2mm Thick Arms with Changes in Number of Stiffeners and a Constant Stiffener Diameter

The third category featured an analysis of the arm assembly with a constant 2mm wall thickness and different number of stiffeners of a constant 1.5mm stiffener diameter. The results from this analysis were compared to the results from the 1.5mm thick arms with a 1.5mm stiffener diameter as presented in Section II. The goal was to analyze how increasing the arm's wall thickness (thereby also increasing the mass) can impact the arm's peak stress. These comparisons would also allow for observation of the effects of changing both wall thickness and number of stiffeners and if a combined change would yield improved results. Table 5 shows the mass of the arms and arm clamps only as well as the total mass of the arm assembly for both the 1.5mm and 2mm thick arms. The total mass of the arm assembly was obtained by adding 1.22kg (combined constant mass of

the six blades, motor, motor shaft, and hub) to the mass of each individual case. Overall, increasing the arm's wall thickness increased the mass of the entire arm assembly by an average of about 3% for each corresponding number of stiffeners than the 1.5mm thick arms.

Table 5. Changes in mass based on various arm wall thicknesses for different numbers of stiffeners

	1.5mm Wall Thickness		2mm Wall Thickness	
Number of Stiffeners	**Mass (kg) Arm + Arm Clamps Only**	**Mass (kg) Arm Assembly**	**Mass (kg) Arm + Arm Clamps Only**	**Mass (kg) Arm Assembly**
6	0.450	1.671	0.501	1.722
8	0.458	1.678	0.509	1.729
10	0.465	1.685	0.517	1.737
12	0.472	1.693	0.525	1.745

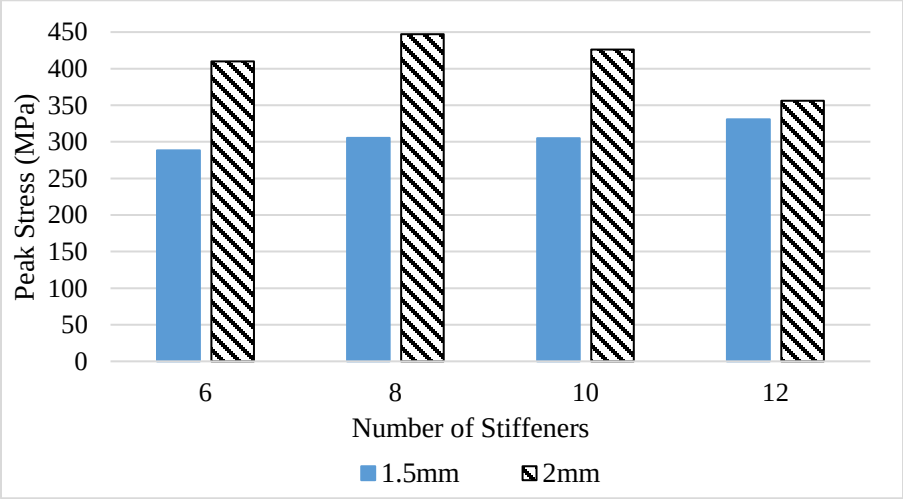

Figure 12. Peak stress trends of an arm assembly with varying wall thicknesses and stiffeners with a constant 1.5mm stiffener diameter

The stress trends for each arm configuration are presented in Figure 12 where the 2mm arms experienced higher stresses than the 1.5mm thick arms, though the peak stress decreased at the highest number of stiffeners. Since the mass of the arms changed with the increasing number of stiffeners, the loading effect was subject to change and as such, the peak stresses in the arm are subject to change significantly especially for the thinner structure. For the modal frequency, Table 6 summarizes the lag and flap frequency modes obtained for each case of the 2mm thick arm assembly as well as the related frequency to mass ratios. Figure 13 and Figure 14 show a comparison between the lag and flap frequency mode trends respectively for the 1.5mm and 2mm thick arms.

Table 6. Frequency to mass ratios of different arm stiffener configurations and a constant 2mm wall thickness

Number of Stiffeners	Mass (kg) Arm + Arm Clamps Only	Lag Mode (Hz)	Lag Frequency to Mass Ratio (Hz/kg)	Flap Mode (Hz)	Flap Frequency to Mass Ratio (Hz/kg)
6	0.501	27.618	55.104	28.348	56.560
8	0.509	27.955	54.900	28.712	56.386
10	0.517	28.285	54.689	29.069	56.205
12	0.525	28.608	54.471	29.416	56.009

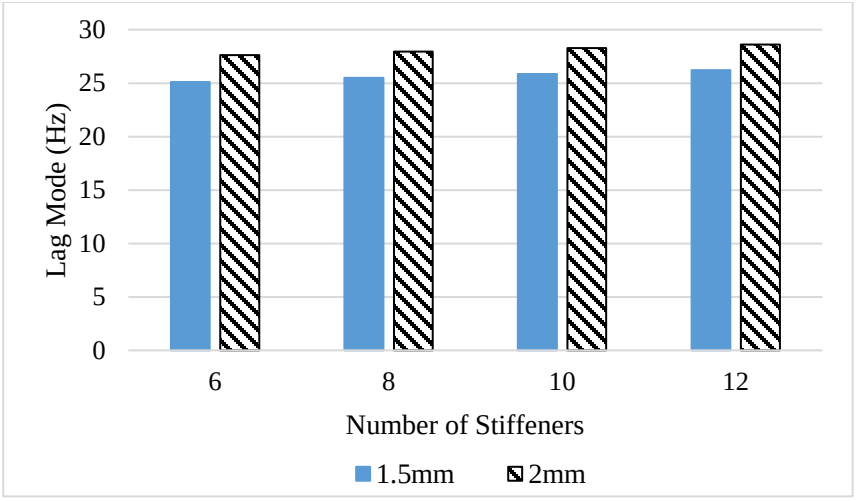

Figure 13. Lag mode for cases of different number of arm stiffeners and wall thicknesses with a constant 1.5mm stiffener diameter

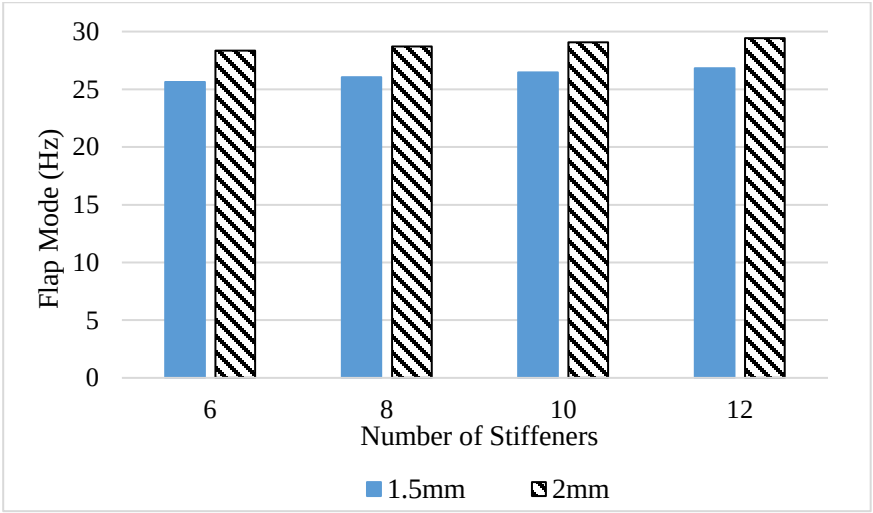

Figure 14. Flap mode for cases of different number of arm stiffeners and wall thicknesses with a constant 1.5mm stiffener diameter

The frequency to mass ratios of the flap and lag frequency modes were only calculated for the 2mm thick arms to determine the category with optimal performance considering mass savings (Figure 15). The 2mm thick arm with six stiffeners performed better with the highest frequency to

mass ratios from both lag and flap frequency modes, that is, with 55.104Hz/kg in lag mode and 56.560Hz/kg in flap mode.

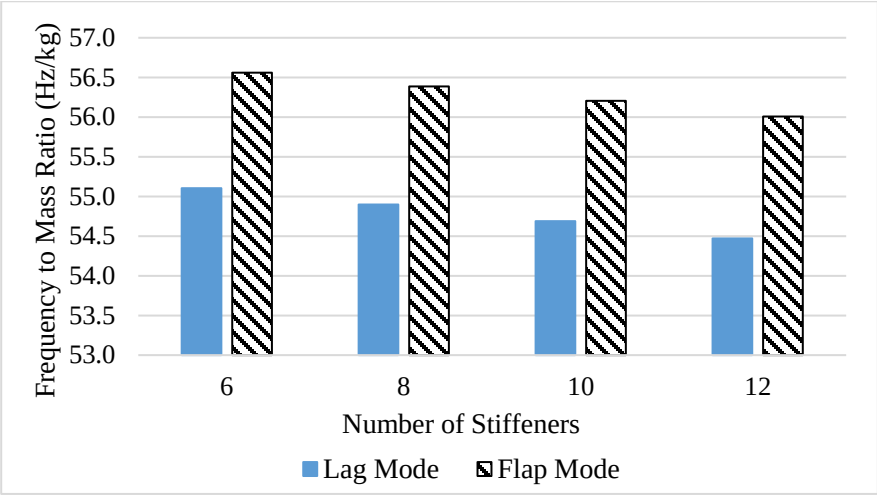

Figure 15. Frequency to mass ratio for cases of different number of arm stiffeners with a 2mm wall thickness and a constant 1.5mm stiffener diameter

IV. Arm Assembly Analysis IV: Simplified MSH Structure for High Fidelity Analyses

Based on the three categories of arm assembly analyses summarized above, the cases selected for further high-fidelity analyses were those which exhibited the best strength and natural frequencies per kg were:

(i) arm assembly with a 1.5mm wall thickness and no stiffeners (the base case)
(ii) arm assembly with ten stiffeners and 0.75mm stiffener diameter at a constant 1.5mm wall thickness, and
(iii) arm assembly with six stiffeners and 1.5mm stiffener diameter at a constant 2mm wall thickness.

The goal for this additional set of analyses was to obtain higher fidelity results beyond a single isolated arm assembly and to particularly observe any interaction between the arm and the fuselage, the arm assembly was added to the fuselage to form a simplified MSH structure, as shown in Figure 16.

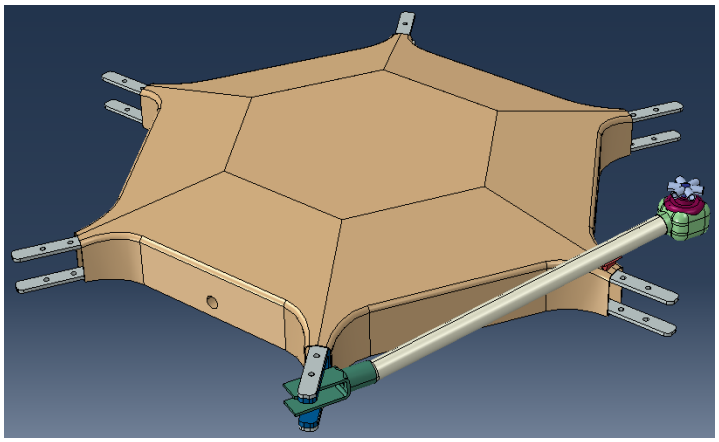

Figure 16. Simplified MSH structure with a singular arm assembly

Additionally, a mesh sensitivity study was performed for each case to identify the smallest mesh size to which the complex shape of the MSH structure could be refined while ultimately providing reasonably higher fidelity peak stress results. For each case, the mesh size was decreased from a coarse mesh to a finer mesh. As the mesh size became finer, the number of elements increased. Following successful meshing, a 26G load was applied to the simplified MSH structure to determine the quasistatic stress. Peak stress results for mesh sensitivity cases were combined and summarized in Figure 17. In the first case regarding the base case 1.5mm thick arms with no stiffeners, the coarse mesh size applied was 0.01 with about 163,000 elements and the finest mesh achieved was 0.002 with over 500,000 elements. At the finest mesh size, the peak stress was around 640MPa. The peak stress for the second case featuring a constant 1.5mm thick arm with ten stiffeners and 0.75mm stiffener diameter initially clustered around the coarse mesh sizes as represented by the lower number of elements (<2,000,000 elements). However, as the number of elements increased to over 5,340,000 elements implying a finer mesh, the peak stress in the arm was about 630MPa.

Lastly, for the third case featuring a constant 2mm thick arm with six stiffeners and 1.5mm stiffener diameter, the peak also clustered around the coarse mesh sizes as represented by the lower number of elements and were relatively low, ranging between 256MPa and 296MPa. However, as the number of elements increased at a finer mesh, the stress in the arm was about 511MPa. Overall, a finer mesh and a higher number of meshed elements was considered more accurate and reliable in capturing localized effects such as stress distributions and deformation patterns in the complex MSH structure. As such, the peak stresses based on the finest mesh size (0.002) were selected for each case. In terms of deformation pattern, peak stresses in the arm were mostly localized in the region on the arm that attaches to the arm support on the frame while in the stowed configuration.

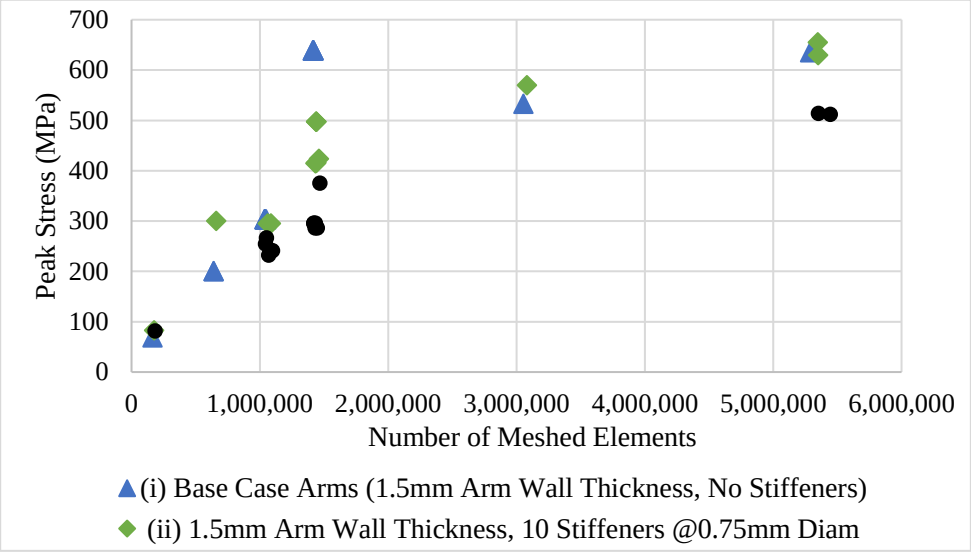

Figure 17. Peak stresses based on mesh refinement of a simplified MSH structure

Furthermore, modal frequency analyses were performed for each case in the deployed configuration to simulate flight operation. Similar to the peak stress analysis, a mesh sensitivity study was performed, and a series of mesh sizes were evaluated up to sixteen refinements. The goal for analyzing different mesh sizes on each arm assembly case was to understand how the frequency varied due to mesh refinement for a higher-fidelity simulation. The possibility of further

refining the mesh was dependent on the number of elements that could be feasibly parsed within the thickness of the arm. As such the finest mesh size allowable for the base case arm assembly was 0.0025 (~3,060,000 mesh elements) and the mesh size for the second and third cases was 0.0035 (~1,470,000 mesh elements). This is important because higher fidelity results that could be extracted from finer mesh sizes were sought. Figure 18 and Figure 19 show the lag and flap frequency mode trends respectively for each arm assembly cases as the mesh size decreases and number of elements increases. It is important to highlight that though the frequency modes, which are close in range, seem clustered into a few data points on each plot, up to sixteen mesh sizes were evaluated. Both lag and flap frequency modes of the arm show a decreasing and asymptotic trend as the mesh is further refined.

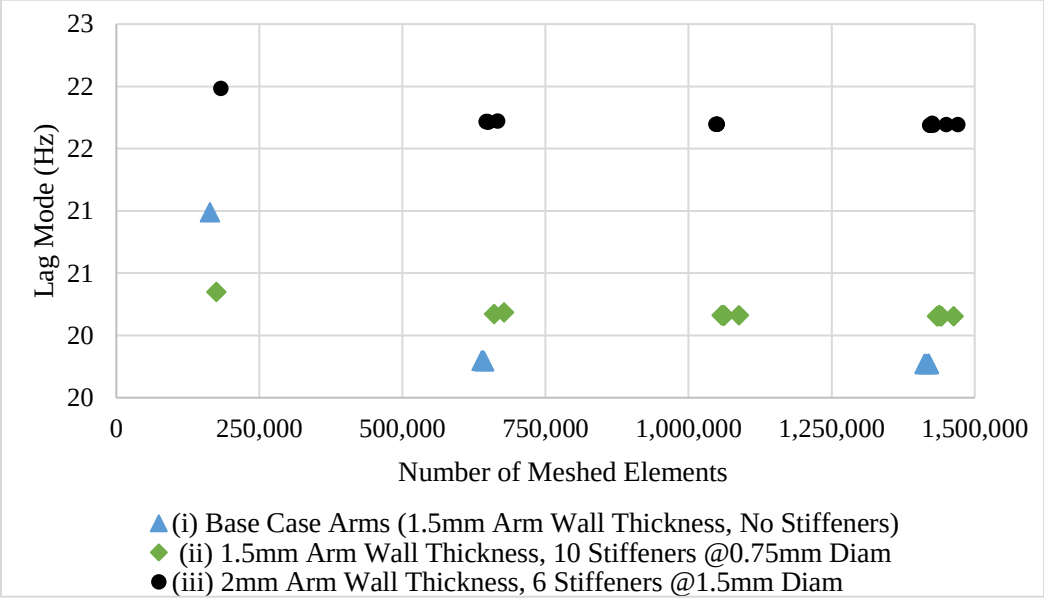

Figure 18. Lag mode trends based on mesh refinement of a simplified MSH structure

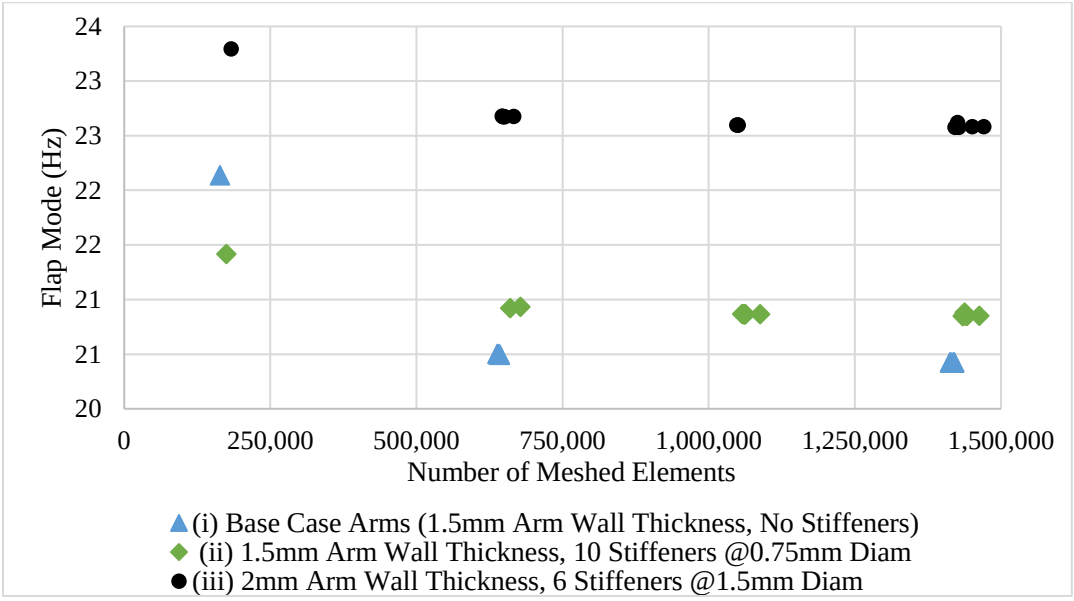

Figure 19. Flap mode trends based on mesh refinement of a simplified MSH structure

The peak stresses as well as the lag and flap frequency modes for each arm assembly case based on the finest mesh size are summarized in Table 7. In terms of optimal structural performance, the base case arm assembly without the stiffeners offered the best performance per weight but had the lowest strength. The arm assembly with six stiffeners and 2mm thick walls offered the lowest stress and highest frequency with only a minimal mass penalty of 73g per arm. These three cases provide a range of options that highlight that depending on the mass margins and desired safety factors for stresses and frequencies; significant improvements can be made in exchange for relatively small mass penalties. Based on the ultimate tensile strength of carbon fiber used in this study, ~1.88GPa, the safety factors for each arm assembly case were calculated to determine how likely the peak stresses are to lie within the allowable limit for the carbon fiber material properties defined. As such, each case had a safety factor > 1 implying a safer structure. It is important to note that for launch loads a safety factor of 1 is satisfactory whereas a safety factor > 3 is satisfactory for operational loads.

Table 7. Results for high-fidelity cases of selected arm configurations on a simplified MSH structure

Wall Thickness (mm)	Number of Stiffeners	Stiffener Diameter (mm)	Mass (kg) Arms + Arms Clamps Only	Peak Stress (MPa)	Factor of Safety	Lag Mode (Hz)	Flap Mode (Hz)
1.5	0	NA	0.4282	640.682	2.93	19.751	20.382
1.5	10	0.75	0.4402	629.087	2.98	20.154	20.850
2.0	6	1.5	0.5012	511.831	3.67	21.693	22.581

III. MSH Frame/Fuselage Study

Besides the rotor arm analysis, other primary load-bearing components of MSH include the frame, fuselage, and landing gear (the landing gear is not discussed in this study). The second MSH load-bearing component analyzed was the MSH frame/fuselage. In the original conceptual design, the frame is the internal structure, and the fuselage is the main body, a large shell that carries and houses the maximum load of MSH including the payload, avionics, electronics, and other instrumentation (Figure 20). A low fidelity MSH structure that included the frame and fuselage and excluded the rotors, motors, hubs, payload, and internal components was created to enable faster iterations with the Abaqus/CAE simulations. Since the mass of interest was only based on the core structural components, the analysis of the low fidelity structure ensured that the frame and fuselage can handle the entire weight of all components as well as survive launch loads and regular flight operation on Mars.

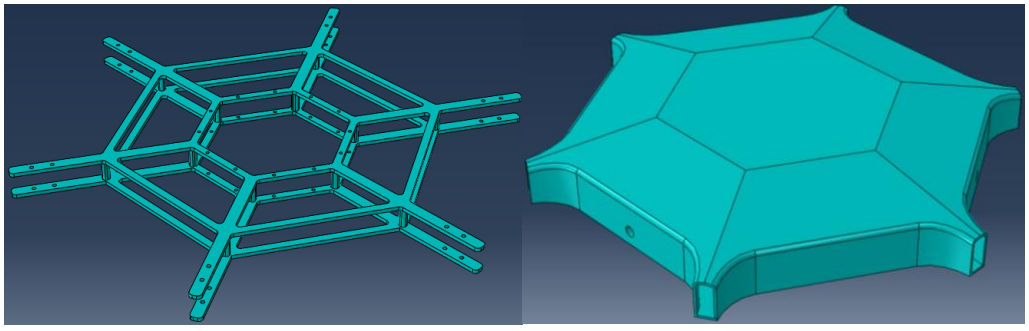

Figure 20. Frame (internal structure) and fuselage of the MSH

In efforts to minimize weight, the frame and fuselage were redesigned such that the new design has the same outer dimensions as the fuselage while replacing the flat frame with a carbon fiber tube frame (Figure 21). The jetpack interface points, the arm supports, the hollow space in the center which houses the payload, and the internal components are subcomponents that were retained in the redesigned tube frame.

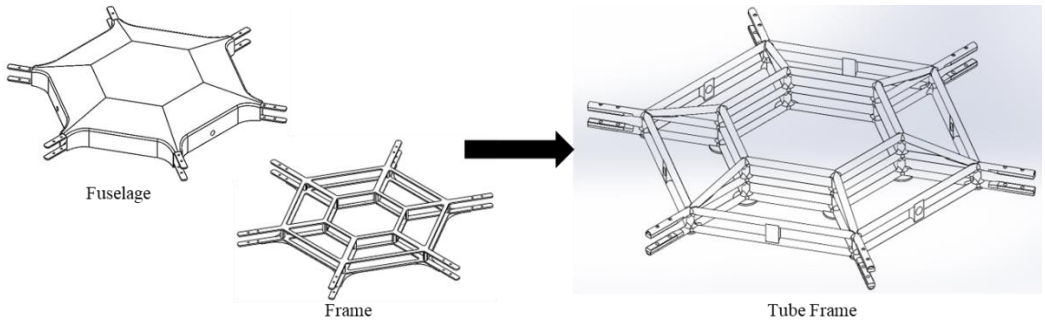

Figure 21. The evolution of the MSH fuselage and frame to a singular tube frame

To ensure a lightweight structure, carbon fiber material properties were assigned to most MSH components, as shown in Table 8, except for the representative motors that were assigned steel material properties thus the mass of the entire MSH structure increased. The mass of each component is based on a baseline 2.5mm frame wall thickness. The masses of the representative payload and internal components were added to represent the casing in which the payload and internal components such as electronics and avionics systems, etc. would be housed. As a more conservative approach, this design assumed higher masses for the MSH structure to account for mass growth allowance and provide more conservative launch loads for the rotorcraft structure.

Table 8. MSH structure material property and mass breakdown

MSH Component	Quantity	Material Properties	Mass (kg)
Leg	4	Carbon fiber (IM7)	0.636
Leg Hinge	4	Carbon fiber (IM7)	0.3656
Arm Cylinder	6	Carbon fiber (IM7)	0.813
Arm Clamp	6	Carbon fiber (IM7)	0.4392
Rotor Clamp	6	Carbon fiber (IM7)	1.194
Motor	6	Steel	7.32
Frame	1	Carbon fiber (IM7)	5.48
Representative Mass of Payload	1	Misc.	11.62
Representative Mass of Internal Components	1	Misc.	12.4
Jetpack Interface Points	3	Carbon fiber (IM7)	0.0519
		Total	40.32

The structural analysis of the tube frame featured three simulation procedures. A quasistatic stress analysis was performed first to determine structural behavior of the tube frame in the stowed configuration when subjected to a 26G load. The three jetpack interface points located at the bottom of the tube frame were fixed with no translation or rotation for the quasistatic 26G analysis. The natural modal frequency of the tube frame in the deployed configuration, depicting flight operation, was also analyzed. An additional quasistatic stress analysis of the tube frame in the

deployed configuration was performed to account for Martian gravity (~0.3G) effects on the MSH. A series of cases for three different categories as presented in Table 9 were analyzed.

Table 9. Categories of parameters and variables defined for the tube frame analysis

Category	Parameters	Variables
1	Frame wall thickness	2mm and 2.5mm
	Arms wall thickness	1.5mm
	Number of arm stiffeners	None
	Arm stiffener diameter	None
2	Frame wall thickness	1mm; 1.5mm; 2mm; 2.5mm
	Arms wall thickness	1.5mm
	Number of arm stiffeners	None
	Arm stiffener diameters	None
3	Frame wall thickness	1mm; 1.5mm; 2mm; 2.5mm
	Arm wall thickness	2mm
	Number of arm stiffeners	6
	Arm stiffener diameter	1.5mm

For each of these categories of analyses, the MSH structure with the new tube frame included the six rotor arm assemblies that is the arm clamp, rotor clamp, and arm cylinder. The rotor blades were excluded but their mass was accounted for in the MSH structure and applied to the motors. In addition, the representative masses for the payload and the internal components were included as shown in Figure 22. The wall thickness was varied to understand the impact of the changing structural mass on the strength of the tube frame when the arms were stowed as well as deployed for flight operation.

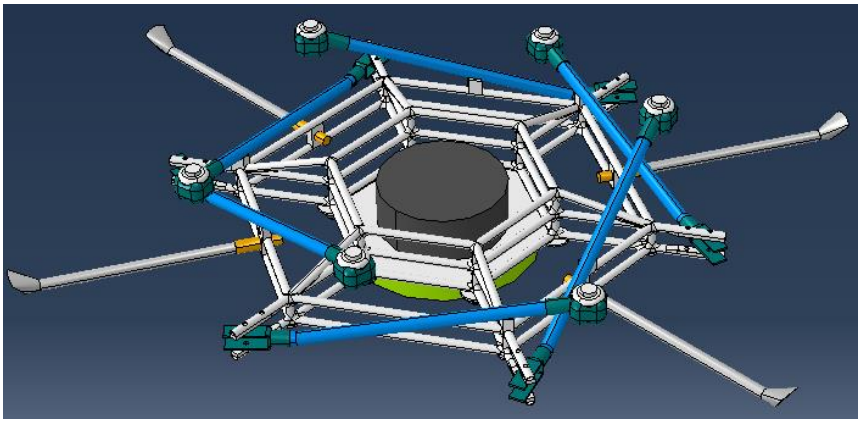

Figure 22. MSH structure showing the new tube frame design

A. MSH Frame/Fuselage Study – Results

I. New Tube Frame Analysis I: Changes in Frame Wall Thickness

The MSH structure was first analyzed in the stowed configuration with the new tube frame at the baseline 2.5mm wall thickness. A mesh sensitivity study was performed such that the mesh size was decreased from a coarse to a finer mesh. The coarser mesh size applied was 0.01 with about 275,000 elements and the finest mesh achieved was 0.003 with over 4,345,000 elements. A finer mesh and a higher number of meshed elements was considered more accurate and reliable in

terms of capturing the stress distributions in the entire MSH structure as well as the frame individually. As such, for a 26G load applied, the peak stresses shown in Figure 23 settled between 450-480MPa for the entire MSH structure and between 330-350MPa for the frame individually based on the three finest mesh sizes considered.

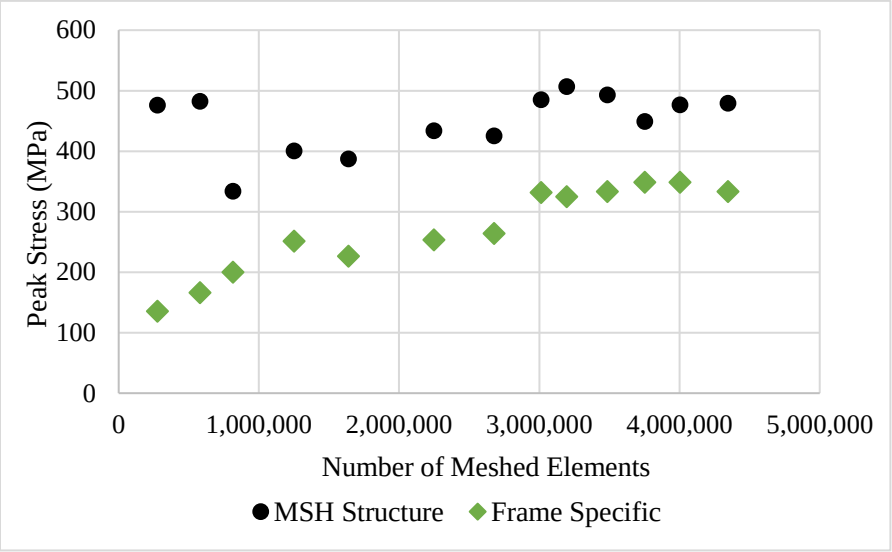

Figure 23. Peak stresses for the entire MSH structure with a 2.5mm thick frame based on mesh refinement

For the modal frequencies of the baseline (2.5mm thick) tube frame, a similar mesh sensitivity study was performed for a series of mesh sizes from a coarse mesh (0.01 = over 275,000 elements) to a finer mesh (0.0032 = over 3,750,000 elements). As shown in Figure 24, the first frequency modes experienced in the tube frame specifically were recorded and for each mesh size, the frequency decreased and leveled at around 74.8Hz at the finest mesh size. Refining the mesh of the MSH structure offered more accurate results in analyzing the frequency at higher fidelity.

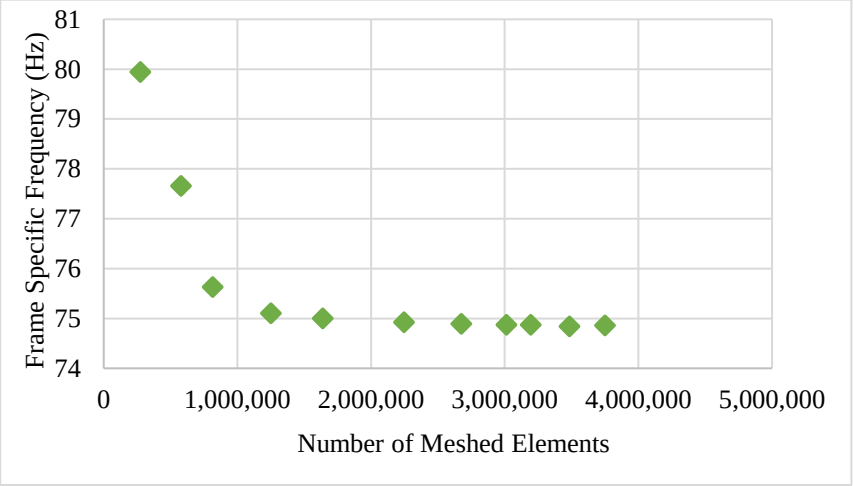

Figure 24. Frame specific frequencies extracted for a series of meshed elements

Following the mesh sensitivity study, the allowable mesh sizes for the stowed configuration (0.0032 = over 3,750,000 elements) and the deployed configuration (0.0034 = over 3,195,000

elements) were selected for optimal analysis and used for the subsequent quasistatic stress and frequency analyses respectively. This was to ensure more accurate results from the finite element simulations. As such, the quasistatic stress of the baseline (2.5mm thick) tube frame was compared to a 2mm thick tube frame. The effect of decreasing the tube frame's wall thickness decreased its total mass and that of the entire MSH structure by 0.63kg as shown in Table 10. The other structural components including the legs, leg hinges, representative masses for the payload and internal components, jetpack interface points and representative motors contributed a combined mass of 34.03kg and six 1.5mm thick arms (baseline arm thickness) contributed a total mass of 0.813kg.

Table 10. Peak stress based on 26G loading and mass comparisons for the MSH structure with various tube frame wall thickness in the stowed configuration

Frame Wall Thickness (mm)	Mass (kg) MSH Structure	Mass (kg) Frame Specific	Peak Stress (MPa) MSH Structure	Peak Stress (MPa) Frame Specific	Factor of Safety (based on Frame)
2.5mm (Baseline)	40.32	5.48	449.129	348.6	5.39
2mm	39.69	4.85	450.356	344.551	5.45

Figure 25 shows that the peak stresses in the entire MSH structure and for the frame specifically. The peak stress in the MSH structure was slightly higher with the thinner frame (2mm). The frame independently, in the stowed configuration, showed a 1.2% decrease in the peak stress. The 2mm thick frame offered the best performance per weight though it yielded lower stress. The ultimate tensile strength of ~1.88GPa for the carbon fiber used in this study was used to calculate the safety factors for the frame. The stresses in each case of frame thickness lie within the allowable limit for the carbon fiber material properties defined and is unique to the mass margins and safety factors required for the design.

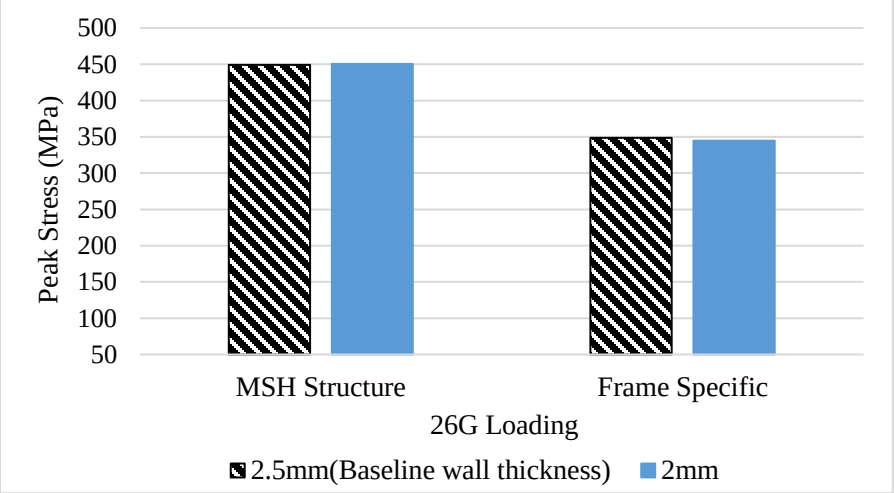

Figure 25. Peak stress trends for various tube frame wall thicknesses in the stowed configuration

In addition, Table 11 and Figure 26 show that the peak stresses of the entire MSH structure in the deployed configuration also slightly increased with the thinner frame (2mm) while the frame independently showed a 30% increase in peak stress. Based on the environmental conditions during the vehicle's operation once deployed, the operational loads result in significantly lower

stresses on the vehicle compared to the launch loads. In this case, stresses under operational conditions are not a major concern but rather the frequency experienced. Regarding the frequency of the frame, the thicker frame had higher frequency which may indicate greater stiffness though it may not imply greater strength due to the larger mass contribution than the thinner frame.

Table 11. Peak stress based on 0.3G loading and mass comparisons for the MSH structure with various tube frame wall thickness in the deployed configuration

Frame Wall Thickness (mm)	Mass (kg) MSH Structure	Mass (kg) Frame Specific	Peak Stress (MPa) MSH Structure	Peak Stress (MPa) Frame Specific	Frequency (Hz) Frame Specific
2.5mm (Baseline)	40.32	5.48	6.495	3.307	16.504
2mm	39.69	4.85	6.496	4.313	16.314

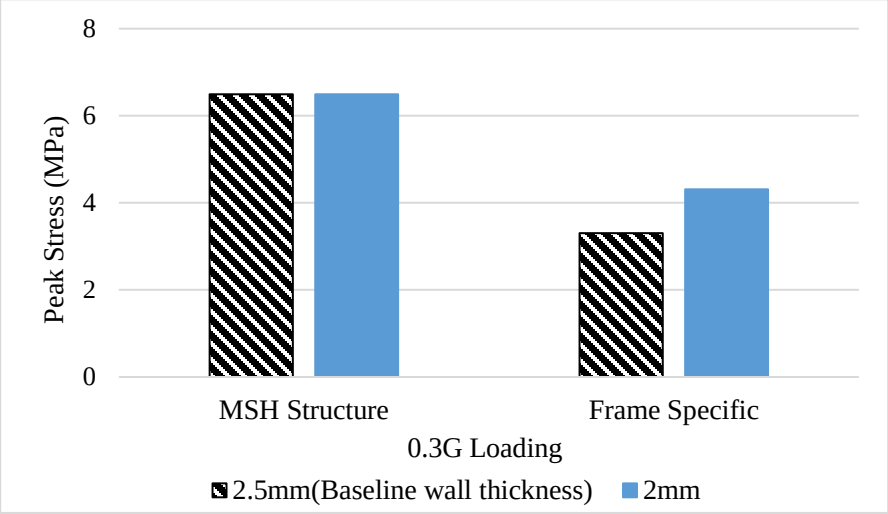

Figure 26. Peak stress trends for the MSH structure with various tube frame wall thicknesses in the deployed configuration

The second and third categories of the tube frame analysis featured the two cases of the better performing arm that is, (I) the arms with no stiffeners and a 1.5mm arm wall thickness (baseline arm assemblies), and (II) the arms with six 1.5mm diameter stiffeners and a 2mm arm wall thickness. The purpose of analyzing the tube frame with two different arm configurations was to potentially obtain high fidelity results of the tube frame's structural behavior along with previously studied arm configurations. For each case the tube frame was analyzed with four different wall thicknesses (1mm, 1.5mm, 2mm, and 2.5mm) in both the stowed and deployed configurations. Note that the change in the frame's wall thickness is directly proportional to the change in the wall's inner diameter. To ensure structural integrity, stability, and manufacturability of the frame, the frame cannot be below a certain wall thickness hence the impact of varying the wall thickness is analyzed to determine feasibility.

II. New Tube Frame Analysis II: MSH Structure Featuring New Tube Frame with Base Case Arm

In the second case of the frame analysis featuring base case arms (constant 1.5mm wall thickness with no stiffeners), a 26G loading was applied to the entire MSH structure in the stowed

configuration to determine the peak stress. Table 12 shows the changes in the mass of the MSH structure and the tube frame independently due to changes in wall thickness. The other structural components including the legs, leg hinges, representative masses for the payload and internal components, jetpack interface points and representative motors contributed a combined mass of 34.03kg and six base case (1.5mm thick) arms contributed a total mass of 0.813kg. Increasing the wall thickness of the frame led to the increase in mass for the tube frame which contributed to the entire mass of the MSH structure. The peak stresses for each change in frame wall thickness are also presented in Table 12. The change in peak stress implies change in the strength of the tube frame based on the wall thickness. As shown in Figure 27, minimum stress was not directly associated to the thickest frame since the loads applied are mass dependent. The thinnest frame wall thickness offered the best performance per weight but had the lowest strength. Similarly, the ultimate tensile strength of ~1.88GPa for the carbon fiber used in this study was used to calculate the safety factors for the frame. The stresses in each case of varying frame thickness lie within the allowable limit for the carbon fiber material properties defined.

Table 12. Peak stress based on 26G loading of the MSH structure featuring different tube frame thicknesses and 1.5mm thick arms in a stowed configuration

Frame Wall Thickness (mm)	Mass (kg) MSH Structure	Mass (kg) Frame Specific	Peak Stress (MPa) MSH Structure	Peak Stress (MPa) Frame Specific	Factor of Safety (based on Frame)
1	38.56	3.72	439.03	329.52	5.70
1.5	39.26	4.42	445.25	308.19	6.1
2	39.86	5.02	440.61	344.90	5.45
2.5	40.42	5.58	446.16	345.33	5.44

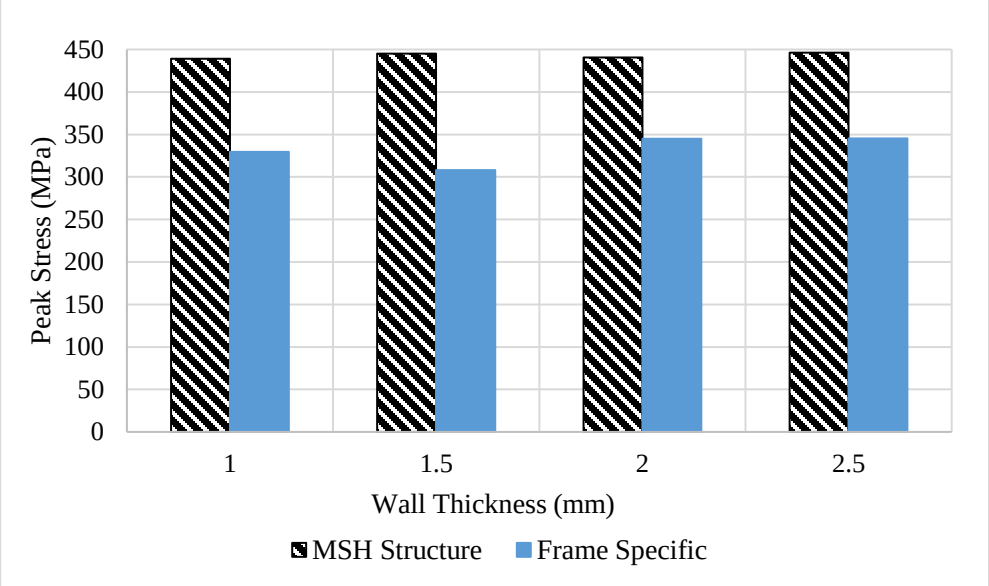

Figure 27. Peak stress trends for the MSH structure with various tube frame wall thicknesses and 1.5mm thick arms in the stowed configuration

Similarly, a 0.3G loading condition was applied to the MSH structure in the deployed configuration to consider flight operation on Mars. The peak stresses shown in Table 13

experienced on the tube frame and the entire MSH structure are significantly lower considering the operational conditions. As the wall thickness and mass of the tube frame increases, the stress decreases hence implying higher strength in the tube frame. It is important to note that in this case, the peak stresses experienced in the frame did not deviate from those experienced in the entire MSH structure besides for the thicker tube frame (2.5mm). Overall, the thinnest tube frame thickness provided better performance per weight from a mass efficiency perspective though had the lowest strength. This is satisfactory for the design parameters employed in this analysis, however, if mission and design requirements and parameters changed, different options of thicknesses would provide more strength.

Table 13. Peak stress based on 0.3G loading of the MSH structure featuring different tube frame thicknesses and 1.5mm thick arms in the deployed configuration

Frame Wall Thickness (mm)	Mass (kg) MSH Structure	Mass (kg) Frame Specific	Peak Stress (MPa) MSH Structure	Peak Stress (MPa) Frame Specific	Frequency (Hz) Frame Specific
1	38.56	3.72	12.88	12.88	13.23
1.5	39.26	4.42	11.27	11.27	14.07
2	39.86	5.02	10.46	10.46	14.57
2.5	40.42	5.58	6.14	5.12	14.88

III. New Tube Frame Analysis III: MSH Structure Featuring New Tube Frame with 2mm Thick Arms and Six Arm Stiffeners

In the third case featuring arms with six stiffeners, 1.5mm stiffener diameter and a constant 2mm arm wall thickness, similar 26G and 0.3G loading conditions were applied to the MSH structure for the stowed and deployed configurations respectively. As the wall thickness increased, the mass of the tube frame increased and, correspondingly, the mass of the MSH structure. Table 14 and Table 15 present the differences in mass, as well as the peak stresses for both the MSH structure and the frame independently. Similarly, the structural components other than the frame of the MSH structure contributed a combined total mass of 34.03kg, and six 2mm thick arms contributed a total of 1.212kg.

As shown in Table 14 and Figure 28, the peak stress changed as the frame wall thickness increased and the minimum stress did not necessarily correlate to the thickest frame. This is because the loads applied are mass dependent which dictates the structural behavior. Similarly, safety factors were obtained for the frame based on the ultimate tensile strength of ~1.88GPa for the carbon fiber used in this study. The stresses in each case of frame thickness lie within the allowable limit for the carbon fiber material properties. Regarding the deployed configuration, the peak stresses as shown in Table 15 were significantly lower due to operating conditions, and the trends show a decrease in stress with increasing thickness. Since the goal is to reduce mass, the thinnest frame turned out to have the best performance per weight though the least strength within acceptable range. It is important to highlight that due to computational limitations, the frequency analysis of the tube frame in this category was not obtained, hence excluded.

Table 14. Peak stress based on 26G loading of the MSH structure featuring different tube frame thicknesses and 2mm thick arms in a stowed configuration

Frame Wall Thickness (mm)	Mass (kg) MSH Structure	Mass (kg) Frame Specific	Peak Stress (MPa) MSH Structure	Peak Stress (MPa) Frame Specific	Factor of Safety (based on Frame)
1	38.96	3.72	368.16	285.92	6.57
1.5	39.66	4.42	324.37	249.51	7.53
2	40.26	5.02	323.99	249.79	7.52
2.5	40.82	5.58	333.07	226.28	8.3

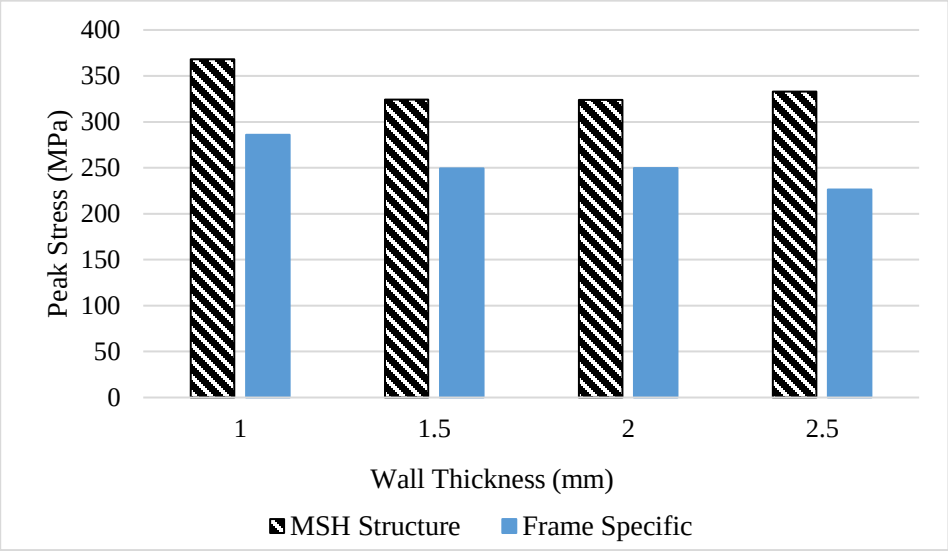

Figure 28. Peak stress trends for the MSH structure with various tube frame wall thicknesses and 2mm thick arms in the stowed configuration

Table 15. Peak stress based on 0.3G loading of the MSH structure featuring different tube frame thicknesses and 2mm thick arms in the deployed configuration

Frame Wall Thickness (mm)	Mass (kg) MSH Structure	Mass (kg) Frame Specific	Peak Stress (MPa) Frame Specific
1	38.96	3.72	13.34
1.5	39.66	4.42	11.58
2	40.26	5.02	10.87
2.5	40.81	5.58	4.76

IV. Implications of the Study and Conclusions

This report highlights the procedures and results from the structural analysis of the Mars Science Helicopter (MSH) load-bearing components that is, the rotor arms and the frame/fuselage. The rotor arms carry and support the rotor system including the blades and the frame/fuselage houses the payload, electronics, and avionics subcomponents. These components are critical to the structure of MSH, and it is important to understand the impact of their structural design on their

performance during launch and under desired operating conditions. The analysis of various rotor arm configurations showed that while a simple tube structure may offer a high frequency/mass ratio while still providing sufficient strength for launch and operational loads, the addition of stiffeners and a thicker wall for the rotor arms is favorable to reduce stresses while not significantly affecting mass margin. By adding the stiffeners and increasing wall thickness, only a small mass penalty of 1.4% of total vehicle mass was observed while structural strength and natural frequencies improved significantly with 20% reduction in peak stress and 10% increase in the natural frequency. The inclusion of stiffeners in the rotor arm also has heritage with the design of the Ingenuity mast and will also reduce deflection of the rotor arms, and consequently reduce changes in the rotor position, during operation. Since the launch loads are acceleration-based, increasing wall thickness also increases mass and consequently the loads and does not necessarily reduce the peak stresses. This behavior is not exhibited as significantly in the rotor arms since the mass of each arm is relatively small in comparison to the much larger frame. Additionally, the fixed mass of the rotor at the end of the arms is a more limiting condition for arms' stresses and is independent of the arm design. While increasing the thickness and number of stiffeners in the arm increased mass on the order of grams, the changes in the frame wall thickness increased the frame mass on the order of kilograms. With 26G loads, mass changes of kilograms results in load changes on the order of hundreds of Newtons, which might be a greater detriment than the benefit gained from increased wall thickness. This behavior is exemplified in the minimum peak stress not being at an extreme wall thickness condition, but at 1.5mm wall thickness.

The transition from the original frame and fuselage design to the single tube frame design significantly reduced mass while also reducing the peak stresses under launch loads. Since the frame is significantly larger than the rotor arms, the peak stresses were not necessarily reduced by increasing wall thickness of the tubes, due to the loads being mass dependent. The analyses showed that a minimum peak stress occurred at a wall thickness of 1.5mm, demonstrating that higher mass components do not have a direct relationship between mass and strength when undergoing launch loads. The rotor arms remained the limiting factor for peak stress experienced under launch loads, although frame thickness does still have an impact on the arm stresses, since the two components are connected. This may suggest that the frame could be made even thinner, but an even thinner frame would be problematic due to its need to remain relatively rigid as it is the critical structural component of the rotorcraft. All cases maintained feasible safety factors, yet there is still margin for further mass reductions. Considering 1mm as the absolute minimum acceptable wall thickness, it is worth assessing the optimal frame wall thickness for the peak stresses on the frame itself. During flight operations, the natural frequency was unique for each case of varying wall thickness. The mass-dependent loads applied impacted the components' peak stresses as well as the natural frequencies.

The overall expected impact from the structural analysis of MSH load-bearing components is to gain increased understanding of the design and loading requirements as well as to improve the weight estimates of some of the major components for a high-payload carrying vehicle. The insights gained through the study of common components under launch loads and operational loads can broadly direct the structural design of components for future rotorcraft development even if the specific design or configuration is altered. Future work may expand these lessons learned by analyzing the impact of structural loads on rotor blades. This would also require experimental blade validation and verification procedures to assess the blades' structural viability.

Acknowledgments

The authors would like to thank the Mars Exploration Program, Dr. William Warmbrodt, and the Aeromechanics Office at NASA Ames Research Center for their guidance and support. Special thanks to Shannah Withrow-Maser, Dr. Gianmarco Sahragard-Monfared, and Dr. Sesi Kottapalli for taking their time to review and provide invaluable feedback.

References

[1] J. Balaram, T. Canham, C. Duncan, M. Golombek, H. F. Grip, W. Johnson, J. Maki, A. Quon, R. Stern and D. Zhu, "Mars Helicopter Technology Demonstrator," *AIAA Atmospheric Flight Mechanics Conference*, Kissimmee, FL, 2018.

[2] J. Balaram, I. J. Daubar, J. Bapst and T. Tzanetos, "Helicopters On Mars: Compelling Science of Extreme Terrains by an Aerial Platform," *Ninth International Conference on Mars*, Pasadena, CA, 2019.

[3] L. Young, L. Pascal, E. Aiken, G. Briggs, G. Pisanich, S. Withrow-Maser and H. Cummings, "The Future of Rotorcraft and other Aerial Vehicles for Mars Exploration," *Vertical Flight Society's 77th Annual Forum & Technology Display*, 2021.

[4] K. Fujita, H. Karaca and H. Nagai, "Parametric Study of Mars Helicopter for Pit Crater Exploration," *AIAA 2020-1734. AIAA SciTech 2020 Forum*, 2020.

[5] S. Withrow-Maser, W. Johnson, L. Young, H. Cummings, A. Chan, T. Tzanetos, J. Balaram and J. Bapst, "An Advanced Mars Helicopter Design," *AIAA Ascend Conference*, Virtual, 2020.

[6] W. Johnson, S. Withrow-Maser, L. Young, C. Malpica, W. J. Koning, W. Kuang, M. Fehler, A. Tuano, A. Chan, A. Datta, C. Chi, R. Lumba, D. Escobar, J. Balaram, T. Tzanetos and H. F. Grip, "Mars Science Helicopter Conceptual Design," NASA/TM—2020–220485, Moffett Field, CA, 2020.

[7] S. Withrow-Maser, W. Johnson, L. Young, W. Koning, W. Kuang, C. Malpica, J. Balaram and T. Tzanetos, "Mars Science Helicopter: Conceptual Design of the Next Generation of Mars Rotorcraft," *AIAA Ascend Conference*, Virtual, 2020.

[8] S. Withrow-Maser, W. Koning, W. Kuang and W. Johnson, "Recent Efforts Enabling Future Mars Rotorcraft Missions," *VFS Aeromechanics for Advanced Vertical Flight Technical Meeting*, San Jose, CA, 2020.

[9] W. Johnson, *Rotorcraft Aeromechanics*, Cambridge University Press, 2013.

[10] W. Koning, W. Johnson and H. F. Grip , "Improved Mars Helicopter Aerodynamic Rotor Model for Comprehensive Analyses," *AIAA Journal*, vol. 57, no. 9, pp. 3969-3979, 2019.

[11] H. F. Grip, C. Malpica, D. P. Scharf, M. Mandić, L. Young, B. Allan, B. Mettler and M. S. Martin, "Flight Dynamics of a Mars Helicopter," *Proceedings of European Rotocraft Forum*, Milan, Italy, 2017.

[12] NASA Jet Propulsion Laboratory, "Combination Methods for Deriving Structural Design Loads Considering Vibro-Acoustic, etc., Responses," Preferred Reliability Practices (Practice No. PD-ED-1211), Pasadena, CA.

[13] R. Blevins, *Formulas for Dynamics, Acoustics and Vibratio*n, West Sussex: John Wiley & Sons, Ltd, 2016.